

# Raman spectroscopic imaging for in vivo detection of cerebral brain metastases

Matthias Kirsch · Gabriele Schackert · Reiner Salzer · Christoph Krafft

Received: 17 May 2010 / Revised: 12 July 2010 / Accepted: 9 August 2010 / Published online: 24 August 2010  
© Springer-Verlag 2010

**Abstract** We report for the first time a proof-of-concept experiment employing Raman spectroscopy to detect intracerebral tumors in vivo by brain surface mapping. Raman spectroscopy is a non-destructive biophotonic method which probes molecular vibrations. It provides a specific fingerprint of the biochemical composition and structure of tissue without using any labels. Here, the Raman system was coupled to a fiber-optic probe. Metastatic brain tumors were induced by injection of murine melanoma cells into the carotid artery of mice, which led to subcortical and cortical tumor growth within 14 days. Before data acquisition, the cortex was exposed by creating a bony window covered by a calcium fluoride window. Spectral contributions were assigned to proteins, lipids, blood, water, bone, and melanin. Based on the spectral information, Raman images enabled the localization of cortical and subcortical tumor cell aggregates with accuracy of roughly 250  $\mu\text{m}$ . This study demonstrates the prospects of Raman spectroscopy as an intravital tool to detect cerebral pathologies and opens the field for biophotonic imaging of the living brain. Future investigations aim to

reduce the exposure time from minutes to seconds and improve the lateral resolution.

**Keywords** In vivo Raman spectroscopy · Brain metastases · Fiber-optic probes · Murine brain tumor model

## Introduction

The principal obstacle during open surgery for intrinsic brain tumors and metastatic deposits of extracranial tumors is the inability to delineate infiltrating tumor from normal tissue. In addition, since the brain has a high functional density, the removal of any lesion is only possible at the very border of the lesion. Safety margins cannot be tolerated as for the treatment of extracerebral diseases. On the other hand, complete removal improves the recurrence-free interval and opens the possibility for adjunct therapeutic strategies. The identification and visualization of residual tumor is, therefore, of paramount importance to improve the outcome of patients with brain tumors.

In general, biophotonic imaging methods give information regarding intrinsic optical properties of tissue and the presence or absence of endogenous or exogenous chromophores. The benefits of using light in imaging living tissue include light providing high sensitivity to functional changes and revealing the dynamics of cells in the nervous system, either via the absorption of light, emission of light, and elastic or inelastic scattering. Further advantages are diffraction-limited spatial resolution in the micrometer, and even submicrometer range, non-destructive sampling, use of non-ionizing radiation, fast data collection, relatively inexpensive instrumentation, and reduced infrastructure requirements compared to other clinical imaging methods. Raman spectroscopy is a biophotonic

M. Kirsch · G. Schackert  
Department of Neurosurgery, Carl Gustav Carus University  
Hospital, Dresden University of Technology,  
Fetscherstr. 74, 01307 Dresden, Germany

R. Salzer · C. Krafft  
Institute of Bioanalytical Chemistry, Dresden University  
of Technology,  
01069 Dresden, Germany

*Present Address:*  
C. Krafft (✉)  
Institute of Photonic Technology,  
Albert-Einstein-Str. 9,  
07745 Jena, Germany  
e-mail: Christoph.krafft@ipht-jena.de

method which probes molecular vibrations based on inelastic scattering of monochromatic radiation. It provides a specific fingerprint of the biochemical composition and structure of tissue without using any labels.

Among the promising applications of biophotonic imaging is the delineation of brain tumor margin *in vivo*. We initiated a research program to detect brain tumors by Raman spectroscopic imaging. Raman images were presented from brain tissue sections [1] and pristine brain tissue [2] and whole mouse brains *ex vivo* [3]. Here, we demonstrated the successful setup for *in vivo* Raman mapping to localize brain metastases.

## Materials and methods

### Murine brain tumor model

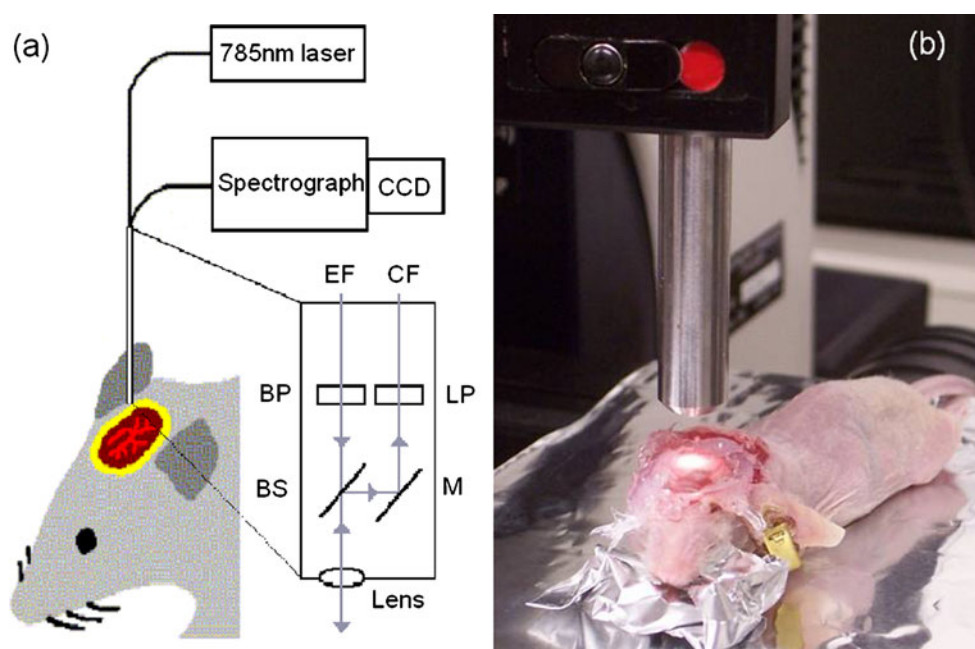
Six- to 8-week-old female NMRI<sup>nu/nu</sup> nude mice were used in a hematogenous brain metastases model [4]. Mice were maintained under pathogen-free conditions according to international and institutional guidelines. Mice were anesthetized by intraperitoneal injection of ketamine and xylazine. Approximately 100,000 tumor cells suspended in 0.1 mL phosphate-buffered salt solution were injected in the right internal carotid artery of the mice, which produced hematogenous brain metastases [5]. Two cell lines were selected: the human melanoma cell line A375 (obtained from American Type Culture Collection, ATCC, Manassas, Virginia, USA) and murine melanoma cell line K1735 (kindly provided by I. Fidler, M.D. Anderson Cancer Center, Houston, Texas, USA). Metastases were allowed

to grow for 3 weeks, until which the mice had symptoms of tumor growth. Five animals were prepared. For cortical *in vivo* imaging, the mice were anesthetized, and via a median skin incision, a bilateral craniotomy was performed which had a diameter of 6–8 mm. The dura was opened and removed, leaving the midline venous sagittal sinus intact. A transparent, 1-mm-thick window made of calcium fluoride was fixed to the skull using zinc phosphate cement (Harvard Dental International GmbH, Hoppegarten, Germany). The procedures were approved by the local and state ethics committees (AZ 24-9168.11-1-2002-11). Melanotic tumors were visible under normal light in two animals, therefore serving as a positive control for Raman spectroscopic findings. Tumors were not found at the cortical surface of the other three animals, and Raman images were not collected from these mice. Following image acquisition, the animals were killed, the brains were removed, embedded in OCT, quickly frozen in a dry ice, and stored at  $-80\text{ }^{\circ}\text{C}$  for histological staining.

### Raman spectroscopic imaging

The experimental setup which is shown in Fig. 1 was similar to an earlier *ex vivo* study of mouse brains [3]. Instead of a filtered fiber-optic probe with a 50- $\mu\text{m}$  excitation fiber and 100- $\mu\text{m}$  collection fiber, a probe with a 100- $\mu\text{m}$  excitation fiber and 200- $\mu\text{m}$  collection fiber was used (both from Inphotonics, USA). A bandpass filter, a beam splitter, a lens, a mirror, and a longpass filter are integrated in the compact probe head. Both fibers had a focal distance of 5 mm. The excitation fiber was connected to a 785-nm diode laser (model BRM-785, BW TEC,

**Fig. 1** Schematic setup of the Raman system used in this study (a). The fiber-optic probe head integrated a bandpass filter (BP), beam splitter (BS), mirror (M), longpass filter (LP), and a lens. The probe was coupled by an excitation fiber (EF) with the laser and by a collection fiber (CF) with the spectrometer. The mouse was placed on a motorized stage to collect Raman images in the mapping mode (b)



USA). The collection fiber was connected to an f/1.8 spectrograph (Kaiser Optical Systems, USA) with a back-illuminated, deep-depletion, liquid nitrogen-cooled CCD detector (Roper Scientific, USA). The larger excitation fiber gave a larger focus of 120  $\mu\text{m}$  as indicated by the manufacturer. Consequently, higher laser intensities of 200 mW could be used for excitation without inducing thermal damages. The larger collection fiber in combination with higher laser intensities enabled reducing the exposure time down to 4 s per spectrum. Raman images were recorded by serial acquisition of spectra at the step size of 100  $\mu\text{m}$  using a motorized sample stage (Prior Scientific, UK). The spectral resolution in the interval 126–3,560  $\text{cm}^{-1}$  was 4  $\text{cm}^{-1}$ . The Raman spectrometer was controlled using HoloGrams (Kaiser) software, which also performed automatic cosmic-ray correction, intensity calibration, and wavenumber calibration. The resulting Raman images were processed by in-house written programs under a Matlab platform (The Mathworks Inc., USA). First, a background was subtracted from each spectrum, then the spectra were normalized by simple multiplicative signal correction, and, finally, the spectra were segmented by k-means cluster analysis in the spectral range 900–1,700  $\text{cm}^{-1}$ . Details have been published previously [6].

## Results

The head of the animal was embedded in a mold of aluminum foil to reduce motion (Fig. 1). However, in future experiments, massive motion artifacts due to pulsations and breathing excursions have to be compensated by rigid fixation using ear bars. We used melanotic tumors to have a reproducible, easily verifiable control in the current proof-of-concept experiments. The presence of melanin is irrelevant to Raman spectroscopic imaging as any tumor has a specific signature. The pigment enabled selecting the areas of interest by visual inspection. The regions were supposed to cross the large midline venous blood vessel and the superior sinus and to cover macroscopically visible tumor as well as normal brain. Photos were recorded using a digital camera for documentation because the fiber probe was not equipped with a white light source and a camera. Two representative examples are shown in Figs. 2 and 3.

As depicted in Fig. 2, the Raman image consisted of 37 $\times$ 33 spectra and probed an area of 3.6 $\times$ 3.2 mm. The sampling area involved the large tumor mass in the right hemisphere, the midline, and the left brain hemisphere (Fig. 2a). The result of the cluster analysis was color coded (Fig. 2b). Normal brain tissue is represented by blue, cyan,

**Fig. 2** Deceased mouse with exposed cortex (a) after Raman spectroscopic images were acquired. The Raman image consisted of 37 $\times$ 33 spectra and probed an area of 3.6 $\times$ 3.2 mm. The sampling area involved the large tumor mass in the right hemisphere, the midline, and the left brain hemisphere. Raman images were segmented by cluster analysis (b) and displayed using false color coding: Normal brain tissue is depicted in *blue, cyan, and yellow*, the *red* midline structures include a central venous blood vessel termed sagittal sinus, and the tumor and tumor margin are shown in *gray* and *black*, respectively. In c, an overlay of the photomicrograph and the Raman image is shown, verifying the correct classification and the macroscopic diagnosis

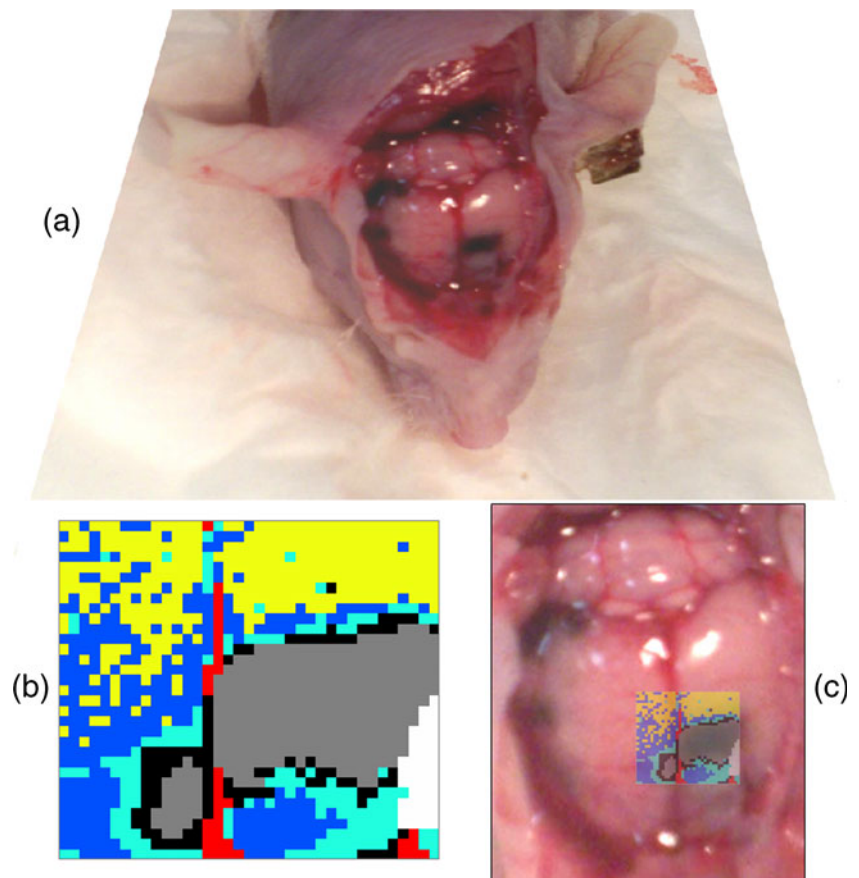
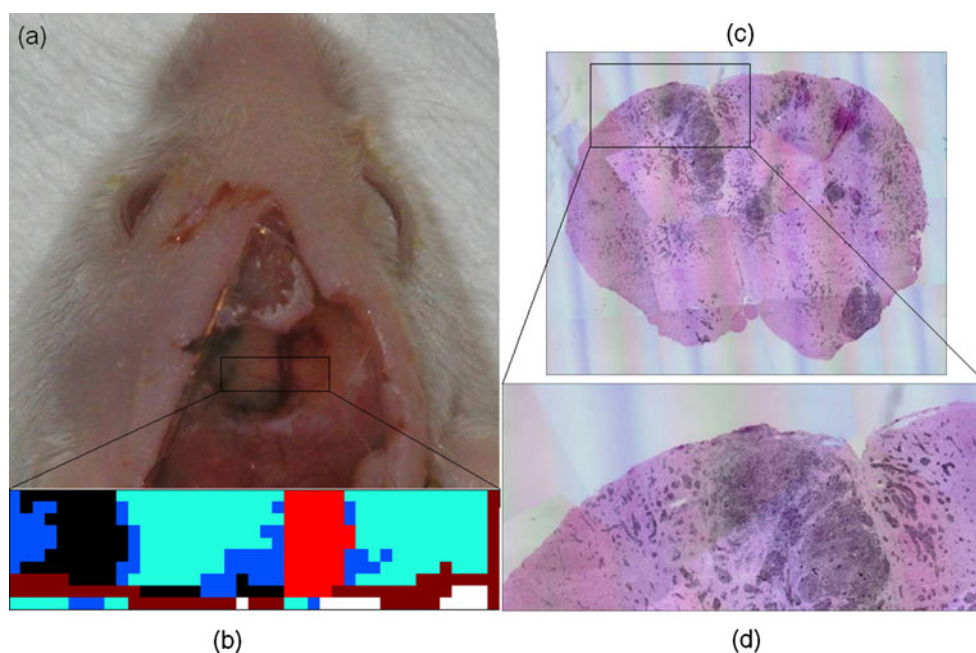




**Fig. 3** Living mouse with cranial window (a). The *box* indicates the area which was studied by Raman imaging. Raman image segmented by cluster analysis (b): normal brain tissue (*blue, cyan*), midline (*red*), bone (*brown*), and tumor (*black*) in the left hemisphere at the border of the analyzed area. An H&E-stained coronal section through the brain is shown in c, the magnification in d



and yellow. The tumor margin is colored black, the midline red, and the main tumor mass gray. An overlay of the Raman image and the photomicrograph is shown in Fig. 2c. It is evident that next to the large tumor mass in the right hemisphere, a small tumor mass is present in the left hemisphere. This small tumor was not visible in the photomicrograph because it was below the surface. The detection of the subsurface tumor demonstrates that Raman spectroscopy is able to penetrate deeper layers in the brain tissue. The exact penetration depth depends on factors such as excitation and collection geometry, the laser wavelength, laser intensity, and tissue composition. In the current backscattering geometry, the accessible depths in living tissue are typically only several hundreds of micrometer. Recently, an approach called spatially offset Raman spectroscopy was introduced, which enables applying the technique as a tomographic tool [7]. The feasibility of 3D tomographic imaging through a canine hind limb with thickness up to 45 mm was demonstrated using transmission Raman spectroscopy [8].

Although the width of the midline was 1 pixel in most parts of the data set, it is difficult to measure the exact spatial resolution on the basis of the cluster analysis results. Here, the lateral resolution was restricted by the data point spacing (100  $\mu\text{m}$ ) and laser focus diameter (120  $\mu\text{m}$ ). Taking these parameters into account together with distortions due to the strongly scattering tissue, the actual lateral resolution can be estimated as roughly 250  $\mu\text{m}$ . Higher lateral resolution would require a smaller data point spacing and a smaller laser focus.

Figure 3a displays how a cranial window was placed on the head of a living mouse. The sampling area is indicated

by a box. Data collection was terminated after  $10 \times 41$  spectra because the mouse had increased motion artifacts that limited further investigations. Cluster analysis of the Raman image (Fig. 3b) resolved a tumor in the left brain hemisphere, the midline harboring a venous vessel termed superior sagittal sinus, bone, and normal brain tissue. The midline is depicted broader than the diameter of the sagittal sinus; in addition, the segmentation is somehow irregular toward the lower portion of the Raman image. This experiment points to the importance of motion artifacts of the mouse head during data acquisition. In forthcoming experiments, the animal will be physically fixed using ear bars and a moth clamp adaptor, which is the usual setup in our laboratory. The corresponding histological hematoxylin and eosin (H&E)-stained coronal section (Fig. 3c, magnification in Fig. 3d) reveals dense and sparse cortical tumor growth, rendering part of the brain surface black. These sections give a rough approximation of gross tumor growth, although they are not exactly orthogonal to the surface.

The Raman spectra in Fig. 4 were averaged without preprocessing or EMSC. For comparison and display in Fig. 4a, the Raman spectra representing the clusters of Fig. 2 have been background-corrected and normalized to the intensity of the band near  $2,933 \text{ cm}^{-1}$ , which is assigned to valence vibrations of  $\text{CH}_2$  and  $\text{CH}_3$  moieties in proteins and lipids. The spectra of normal brain tissue slightly differ in the intensities of valence vibrations of OH bonds near  $3,245$  and  $3,425 \text{ cm}^{-1}$  that are mainly assigned to water. Therefore, the different classifications of normal brain might be due to various amounts of water overlying the curved murine brain. In order to provide a good contact between tissue and the calcium fluoride window, a drop of

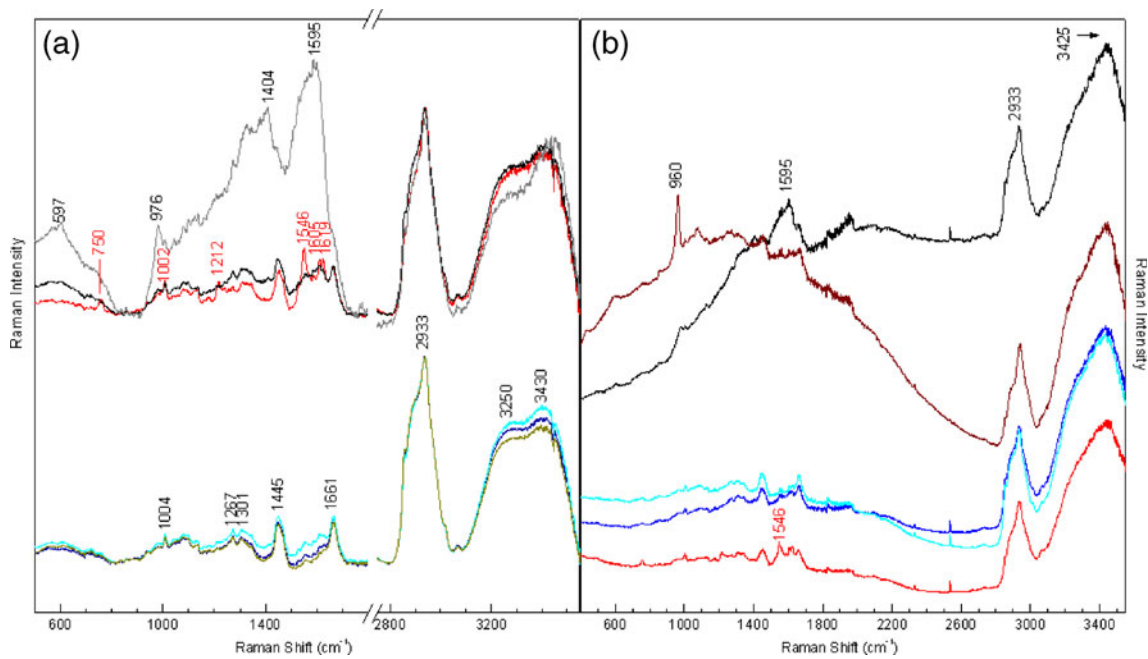


**Fig. 4** Raman spectra corresponding to the clusters in Figs. 2a and 3b. Spectra were baseline-corrected, normalized, and shifted for overlay in two groups (a). Unprocessed spectra are displayed in b

aqueous buffer was applied to the exposed brain. This procedure could affect the water content, and, consequently, the spectral range was not considered for cluster analysis and the region from 900 to 1,700  $\text{cm}^{-1}$  was used instead because it contains only a weak Raman band of water near 1,640  $\text{cm}^{-1}$ . In general, bands in the lower wavenumber region from 500 to 1,800  $\text{cm}^{-1}$  show lower intensities. Most prominent bands are assigned to the aromatic amino acid phenylalanine (1,004  $\text{cm}^{-1}$ ), unsaturated fatty acids (1,267 and 1,661  $\text{cm}^{-1}$ ),  $\text{CH}_2$  and  $\text{CH}_3$  deformation vibrations (1,301 and 1,445  $\text{cm}^{-1}$ ), and the amide bands of protein backbones (1,267 and 1,661  $\text{cm}^{-1}$ ) that overlap with spectral contributions of fatty acids. The Raman spectrum of the midline contains additional bands due to oxygenated hemoglobin near 750, 1,002, 1,212, 1,546, 1,605, and 1,619  $\text{cm}^{-1}$ . The intensities of these bands are enhanced due to a resonance effect known as resonance Raman spectroscopy. This is caused by the chromophore heme of the hemoglobin molecule which partly absorbs the excitation radiation, resulting in increased Raman cross-sections of heme-associated vibrations.

The Raman spectrum of the tumor displays additional spectral contributions due to the pigment melanin near 597, 976, 1,404, and 1,595  $\text{cm}^{-1}$ , which has also previously been found [3]. The Raman resonance enhancement amplifies the intensities, so the bands in the lower wavenumber region are even more intense than in the higher wavenumber region. The pigment is expressed by tumor cells and can be used as an inherent marker of these brain metastases. In the Raman spectrum of the tumor margin,

spectral contributions of normal brain tissue and the pigment melanin overlap, indicating the infiltrative nature of tumor growth independent of its visibility. Furthermore, scattering from subsurface tumor portions might be responsible for weak spectral contributions of melanin in the spectrum of the cyan cluster of Fig. 4a. It cannot be excluded that the limited lateral resolution might give mixed clusters. That means the fiber probe excites and collects both tissues simultaneously at the transition between tumor and normal brain.

The Raman spectra representing the clusters in Fig. 3 are included in Fig. 4b. Here, the unprocessed spectra are displayed, which means without background correction and normalization. The Raman spectrum of the midline venous sagittal sinus is characterized by the lowest background and spectral contributions of hemoglobin. On an overall perspective, the background of normal brain tissue is obviously increased. As before, these spectra are dominated by spectral contributions of proteins, lipids, and water. Autofluorescence is not an issue for normal brain tissue and blood with 785-nm excitation. The background is increased in the spectra representing the brown and the black clusters. A band at 960  $\text{cm}^{-1}$  in the Raman spectrum of the brown cluster is typical for hydroxyapatite of bone. The enhanced spectral contributions of the pigment melanin in tumor cells are accompanied by the highest background. Such a background is consistent with fluorescence emission, which is simultaneously excited by the laser. The overlap with fluorescence is even more problematic using excitation lasers in the wavelength range 400–700 nm. This is the main reason

to select a near-infrared (NIR) laser with 785-nm emission as excitation source. In addition, the lower absorption of NIR radiation in tissues is advantageous to penetrate deeper sections of the tissue, as demonstrated for subsurface tumor detection in Fig. 2.

## Discussion

Intense NIR lasers, innovative optical filters, and sensitive detectors were developed in the past and improved the sensitivity of Raman spectroscopy for biomedical studies (reviewed in [9]). The potential implications of *in vivo* Raman spectroscopy for online diagnostic purposes and guidance of therapies are promising. Due to technical limitations, most previous *in vivo* Raman studies simply recorded single spectra. *In vivo* applications have been reported to detect dysplasia in the rat palatum [10] and in the human gastrointestinal tract [11], precancers in the cervical epithelium [12], lesions of breast tissue [13], and polyps in colon [14] and to determine the molecular composition of artery wall [15]. Another *in vivo* study reported the detection of glioma brain tumors by Raman microscopy coupled to a microprobe [16]. The authors induced brain tumors in rats by direct injecting tumor cells in the brain. Tissue sections from this tumor model were previously studied by Raman spectral imaging [17]. In contrast, our proof-of-concept study obtained Raman images from the brains of living mice. Raman images enabled the identification of cortical and subcortical tumors, therefore visible and invisible tumors to the unshielded eye. The reported probe geometries [10–16] used excitation fibers with diameters of more than 200  $\mu\text{m}$ , which gave a laser focus diameter of more than 200  $\mu\text{m}$  depending on the numerical aperture. The lensed fiber-optic probe in this study had a smaller focus diameter near 100  $\mu\text{m}$ , which enabled, in combination with a step size of 100  $\mu\text{m}$ , a lateral resolution of roughly 250  $\mu\text{m}$ . The resolution of these probes is not sufficient to identify single cells. From a clinical point of view, single cell resolution is beyond surgical capabilities and—if adopted as a standard—needs to be combined with an automated cell-based therapeutic strategy such as single cell laser ablations. Relevant surgical dexterity ranges from 100 to 1,000  $\mu\text{m}$  if an operating microscope is used. Usually, tumor margins within the brain parenchyma can be estimated to a level of 1–3 mm, although this depends on purely visual inspection—better diagnostics would improve the surgical capabilities. The focused laser beam could induce carbonization and significant spectral changes if the local intensity is above the damage threshold. However, we concluded from the unchanged and non-distorted spectra that no visible thermal damage occurred. In addition, H&E staining

did not reveal any burning in the measured area of living mice. Viable tissue is able to dissipate absorbed thermal energy to a greater extent than non-viable tissue. Prior to clinical application, toxic levels of laser irradiation have to be defined in more detail. Obviously, an exposure time of 4 s per spectrum and image acquisition in the serial mapping mode adding up to a total exposure of several minutes are impractical in intraoperative clinical applications. A technology that can be used in a clinical setting should either perform an automated scan or use navigated mapping of, e.g., a resection cavity. Therefore, the scope of further developments is to reduce exposure time and to increase lateral resolution.

The fiber-optic Raman probe from Inphotonics, which was used in this study, is too large for endoscopic applications. Miniaturized fiber-optic probes are required for use with endoscopes. In spite of more than 10 years of development by numerous research groups, such fiber-optic probes for biomedical application are not commercially available yet. A new mini-fiber-optic Raman probe suitable for insertion into the working channel of a bronchoscope from Emvision LCC (USA) was recently introduced and might fill the gap [18]. To avoid the technical complexity of Raman probes, unfiltered fused silica fibers have been introduced to probe the high wavenumber region from 2,400 to 3,800  $\text{cm}^{-1}$  [19] and applied for Raman spectroscopic characterization of porcine brain tissue [20]. Even more useful for Raman imaging would be a probe made of fiber bundles. A similar probe was recently introduced for fluorescence imaging [21] which enables collecting images from brains of freely moving mice. In the current clinical environment, spectroscopic information could be introduced as part of multimodal imaging to guide brain tumor resection and visualize normal from infiltrated cancerous brain.

In general, a common set of classification algorithms need to be developed that can cover a broad range of pathologies. We have previously shown that the different grades of gliomas can be distinguished by optical spectroscopy, as well as various substructures within the normal human, porcine, and murine brain [3, 22, 23]. Another recent report demonstrated Raman spectroscopic classification of rat brain hippocampus suffering from Alzheimer's disease [24]. Therefore, additional applications are the biochemical verification of target areas not only of tumors but also, e.g., stereotactic operations guided by a fiber-optic device for degenerative lesions, such as in Parkinson's disease.

Alternative photonic methods are under investigation to offer intravital measurements. Nonlinear variants of Raman spectroscopy such as coherent anti-Stokes Raman scattering (CARS) and stimulated Raman scattering (SRS) offer signal enhancement of several orders of magnitude. CARS

was already applied in the context of brain tumors [25]. SRS is a new approach which was recently demonstrated for lipid vesicles in single cells [26]. In combination with laser scanning microscopes, images can be acquired at video time frame rates with diffraction-limited lateral resolution. Linear Raman spectroscopy is still a valuable experimental tool because in contrast to CARS and SRS, Raman spectra offer full spectral information [27]. Future progress in nonlinear Raman spectroscopy and fiber probe development will pave the way to enable promising prospects of Raman spectroscopy in diagnostic applications. The next step in our research program is to localize and monitor growth of brain metastases of various primary organs in living mice.

**Acknowledgments** We would like to thank Dr. Daniel Martin and Dipl. Biol Elke Leinertz for their help. The research is funded by the German Research Foundation (DFG) within the project “Real time diagnosis of brain metastasis in animal models using Raman imaging” and by the MedDrive Start-up funds of the Medical Faculty, Dresden University of Technology.

## References

- Krafft C, Sobottka SB, Schackert G, Salzer R (2006) Raman and infrared spectroscopic mapping of human primary intracranial tumors: a comparative study. *J Raman Spectrosc* 37:367–375
- Krafft C, Sobottka SB, Schackert G, Salzer R (2005) Near infrared Raman spectroscopic mapping of native brain tissue and intracranial tumors. *Analyst* 130:1070–1077
- Krafft C, Kirsch M, Beleites C, Schackert G, Salzer R (2007) Methodology for fiber-optic Raman mapping and FTIR imaging of metastases in mouse brains. *Anal Bioanal Chem* 389:1133–1142
- Schackert G, Fidler IJ (1988) Development of in vivo models for studies of brain metastasis. *Int J Cancer* 41:589–594
- Kirsch M, Weigel P, Pinzer T, Carroll RS, Black PM, Schackert HK, Schackert G (2005) Therapy of hematogenous melanoma brain metastases with endostatin. *Clin Cancer Res* 11:1259–1267
- Krafft C, Codrich D, Pelizzo G, Sergio V (2008) Raman and FTIR imaging of lung tissue: methodology for control samples. *Vib Spectrosc* 46:141–149
- Matousek P, Morris MD, Everall N, Clark IP, Towrie M, Draper E, Goodship A, Parker AW (2005) Numerical simulations of subsurface probing in diffusely scattering media using spatially offset Raman spectroscopy. *Appl Spectrosc* 59:1485–1492
- Schulmerich MV, Cole JH, Dooley KA, Morris MD, Kreider JM, Goldstein SA, Srinivasan S, Pogue BW (2008) Noninvasive Raman tomographic imaging of canine bone tissue. *J Biomed Opt* 13:020506
- Krafft C, Dietzek B, Popp J (2009) Raman and CARS microspectroscopy of cells and tissues. *Analyst* 134:1046–1057
- Bakker Schut TC, Witjes MJ, Sterenborg HJ, Speelman OC, Roodenburg JL, Marple ET, Bruining HA, Puppels GJ (2000) In vivo detection of dysplastic tissue by Raman spectroscopy. *Anal Chem* 72:6010–6018
- Huang Z, Bergholt MS, Zheng W, Lin K, Ho KY, The M, Yeoh KG (2010) In vivo early diagnosis of gastric dysplasia using narrow-band image-guided Raman endoscopy. *J Biomed Opt* 15:037017
- Utzinger U, Heintzelmann DL, Mahadevan-Jansen A, Malpica A, Follen M, Richards-Kortum R (2001) Near-infrared Raman spectroscopy for in vivo detection of cervical precancers. *Appl Spectrosc* 55:955–959
- Motz JT, Gandhi SJ, Scepanovic OR, Haka AS, Kramer JR, Dasari RR, Feld MS (2005) Real-time Raman system for in vivo disease diagnosis. *J Biomed Opt* 10:031113
- Molckovsky A, Song LM, Shim MG, Marcon NE, Wilson BC (2003) Diagnostic potential of near-infrared Raman spectroscopy in the colon: differentiating adenomatous from hyperplastic polyps. *Gastrointest Endosc* 57:396–402
- Buschman HP, Marple ET, Wach ML, Bennett B, Schut TC, Bruining HA, Bruschke AV, van der Laarse A, Puppels GJ (2000) In vivo determination of the molecular composition of artery wall by intravascular Raman spectroscopy. *Anal Chem* 72:3771–3775
- Beljebbar A, Dukic S, Amharref N, Manfait M (2010) Ex vivo and in vivo diagnosis of C6 glioblastoma development by Raman spectroscopy coupled to microprobe. *Anal Bioanal Chem* 398:477–487
- Amharref N, Beljebbar A, Dukic S, Venteo L, Schneider L, Pluot M, Manfait M (2007) Discriminating healthy from tumor and necrosis tissue in rat brain tissue samples by Raman spectral imaging. *Biochim Biophys Acta* 1768:2605–2615
- Magee ND, Villaumie JS, Marple ET, Ennis M, Elborn JS, McGarvey JJ (2009) Ex vivo diagnosis of lung cancer using a Raman miniprobe. *J Phys Chem B* 113:8137–8141
- Santos LF, Wolthuis R, Koljenovic S, Almeida RM, Puppels GJ (2005) Fiber-optic probes for in vivo Raman spectroscopy in the high-wavenumber region. *Anal Chem* 77:6747–6752
- Koljenovic S, Bakker Schut TC, Wolthuis R, Vincent AJPE, Hendriks-Hagevi G, Santos LF, Kros JM, Puppels GJ (2007) Raman spectroscopic characterization of porcine brain tissue using a single fiber-optic probe. *Anal Chem* 79:557–564
- Flusberg BA, Nimmerjahn A, Cocker ED, Mukamel EA, Barretto RP, Ko TH, Burns LD, Jung JC, Schnitzer MJ (2008) High-speed, miniaturized fluorescence microscopy in freely moving mice. *Nat Methods* 5:935–938
- Dreissig I, Machill S, Salzer R, Krafft C (2009) Quantification of brain lipids by FTIR spectroscopy and partial least squares regression. *Spectrochim Acta A Mol Biomol Spectrosc* 71:2069–2075
- Kohler M, Machill S, Salzer R, Krafft C (2009) Characterization of lipid extracts from brain tissue and tumors using Raman spectroscopy and mass spectrometry. *Anal Bioanal Chem* 393:1513–1520
- Chen P, Shen A, Zhao W, Baek SJ, Yuan H, Hu J (2009) Raman signature from brain hippocampus could aid Alzheimer's disease diagnosis. *Appl Opt* 48:4743–4748
- Evans CL, Xu X, Kesari S, Xie XS, Wong ST, Young GS (2007) Chemically-selective imaging of brain structures with CARS microscopy. *Opt Express* 15:12076–12087
- Freudiger CW, Min W, Saar BG, Lu S, Holtom GR, He C, Tsai JC, Kang JX, Xie XS (2008) Label-free biomedical imaging with high sensitivity by stimulated Raman scattering microscopy. *Science* 322:1857–1861
- Krafft C, Ramoji AA, Bielecki C, Vogler N, Meyer T, Akimov D, Rosch P, Schmitt M, Dietzek B, Petersen I, Stallmach A, Popp J (2009) A comparative Raman and CARS imaging study of colon tissue. *J Biophotonics* 2:303–312